ADVANCED FUNCTIONAL MATERIALS
www.afm-journal.de

Outstanding Room-Temperature Thermoelectric Performance of n-type Mg_3Bi_2-Based Compounds Through Synergistically Combined Band Engineering Approaches

*Hyunyong Cho, Song Yi Back, Naoki Sato, Zihang Liu, Weihong Gao, Longquan Wang, Hieu Duy Nguyen, Naoyuki Kawamoto, and Takao Mori**

Thermoelectric cooling materials based on Bi_2Te_3 have a long history of unsurpassed performance near room temperature. Recently, research into price-competitive $Mg_3(Bi, Sb)_2$-based materials are focused on replacing traditional cooling materials. Here, the thermoelectric properties of $Mg_{3.2}Bi_{1.998-x}Sb_xTe_{0.002}Cu_{0.005}$ (x = 0.0, 0.1, 0.2, 0.3, 0.4, and 0.5) polycrystalline compounds are investigated. In all temperature regions, electrical resistivity and Seebeck coefficient are increased with Sb concentration. The electronic transport properties of Sb-alloyed compounds are maximized by synergistically combined band engineering approaches such as band structure change caused by lattice strain, increased electronic density of states, and chemical potential shift, leading to exceptionally high-power factor values of over 3.0 mW m^{-1} K^{-2} at room temperature. Furthermore, with increasing Sb content, thermal conductivity values are systematically reduced due to the promotion of alloy scattering of phonons and suppression of the bipolar contribution. Consequently, these multiple approaches significantly enhance thermoelectric performance, resulting in an enhancement of thermoelectric figure-of-merit zT above 1.1 at 348–423 K. Additionally, a zT_{avg} of 1.1 is recorded at 300–450 K, making it an unrivaled value among the reported n-type Mg_3Bi_2-based thermoelectric materials. Overall, this work demonstrates that Mg_3Bi_2-based materials are more promising for thermoelectric cooling applications compared to Bi_2Te_3-based materials.

1. Introduction

Global climate change has been demanding the mitigation of growing environmental and energy crises, which is spurring rapid progress in clean and efficient energy conversion technologies. Among them, thermoelectric technology can directly convert heat into electricity and vice versa. Thermoelectric (TE) devices, including no pollution, noiseless, and high reliability, offer a great opportunity for solid-state cooling and alternative energy-saving system.[1,2] The performance of TE materials is characterized by the dimensionless figure of merit zT, which is defined by $zT = S^2 T/\rho(\kappa_{lat} + \kappa_e)$, where S, T, ρ, κ_{lat}, and κ_e are the Seebeck coefficient, absolute temperature, electrical resistivity, lattice thermal conductivity, and electronic thermal conductivity, respectively. There are several well-known conventional strategies for improving thermoelectric performance. For example, a great deal of effort has been made to lower the lattice thermal conductivity by inducing scattering of phonons from point defects, lattice strain, dislocation, nanograin, and nanoprecipitates.[3–9] In addition, several effective strategies have been adopted to optimize the power factor ($PF = S^2/\rho$) by achieving band engineering, optimizing carrier concentration, utilizing magnetism, suppressing bipolar contribution, and introducing low energy carrier filtering.[10–17]

With a long history over the past decades, Bi_2Te_3-based compounds are well-known for their excellent TE material near room temperature and are mainly used for solid-state cooling.[18,19] However, the scarcity of tellurium element makes it expensive to manufacture more applications. Therefore, there is a

H. Cho, H. D. Nguyen, N. Kawamoto
Center for Basic Research on Materials
National Institute for Materials Science (NIMS)
1-1 Namiki, Tsukuba, Ibaraki 305-0044, Japan

The ORCID identification number(s) for the author(s) of this article can be found under https://doi.org/10.1002/adfm.202407017

DOI: 10.1002/adfm.202407017

S. Y. Back, N. Sato, Z. Liu, W. Gao, L. Wang, T. Mori
Research Center for Materials Nanoarchitectonics (MANA)
National Institute for Materials Science (NIMS)
1-1 Namiki, Tsukuba, Ibaraki 305-0044, Japan
E-mail: MORI.takao@nims.go.jp

T. Mori
Graduate School of Pure and Applied Science
University of Tsukuba
1-1-1 Tennodai, Tsukuba, Ibaraki 305-8671, Japan

need for a material that can replace Bi_2Te_3-based compounds while having low-cost and high thermoelectric performance near room temperature. The discovery of high-performance n-type Mg_3Sb_2-based materials in the mid-temperature region caused a great sensation in the thermoelectric community.[20] Alloying Mg_3Bi_2 with Mg_3Sb_2 provides strengthened phonon scattering and modified band structure, resulting in high thermoelectric performance.[21] Experientially, as the Bi content increases, the maximum zT value shifts toward lower temperatures, favoring near-room temperature application. Recently, Mg_3Bi_2-based compounds have attracted great attention as potential replacements of traditional Bi_2Te_3. Mao et al. reported that Mg_3Bi_2-based compounds have a great deal of potential as thermoelectric cooling materials.[22] Since then, several efforts to maximize their thermoelectric performance near room temperature have continued until recently. As reported by Liu et al., the TE performance of $Mg_{3.2}Bi_{1.5}Sb_{0.498}Te_{0.002}Cu_{0.01}$ was successfully maximized by precisely controlling the microstructure to induce rapid changes in their carrier mobility.[23] Furthermore, a high performance of Y-doped $Mg_{3.6}Bi_{1.4}Sb_{0.6}$ system was achieved by effectively mitigating the grain-boundary scattering of charge carriers.[24]

Normally, in the Mg_3Bi_2-Mg_3Sb_2 alloy systems, band engineering has been adopted as one of the useful strategies to enhance their performance[11,22] because Mg_3Bi_2 compound has a semimetal behavior which typically has been considered disadvantageous in TE applications.[25,26] Recently, it has been also been considered to be a Nodal-line semimetal. Therefore, modifying the band structure, such as opening the band gap, by controlling the amount of Sb is necessary to obtain a better TE performance. Band convergence and band alignment, which dramatically increases valley degeneracy, are other representative examples of band engineering.[27,28] One of the effects of band engineering is that the PF can be improved by increasing weighted mobility (μ_w), which is proportional to valley degeneracy (N_V).[29,30] This means that high N_V values can effectively improve thermoelectric properties. The lowest conduction band of Mg_3Bi_2 compound is located along L*-M*line with six-folded valley degeneracy ($N_V = 6$) and there is a single-valley conduction band ($N_V = 1$) at Γ point.[14,25,26,31–33]

Here, we report the thermoelectric properties of $Mg_{3.2}Bi_{1.998-x}Sb_xTe_{0.002}Cu_{0.005}$ (hereafter referred to as Sbx, x = 0.0, 0.1, 0.2, 0.3, 0.4, and 0.5). The state-of-the-art power factor values among the Mg_3Bi_2-based system exceeding 3.0 mW m^{-1} K^{-2} near room temperature were obtained for Sb0.3, Sb0.4, and Sb0.5 through a highly effective band engineering realizing high μ_w. Furthermore, we found quite a few lattice strains in the microstructure of the present compounds due to nanopores generated by the evaporation of excess Mg content during the sintering process. Through the theoretical band structure calculation, it was discovered that the lattice strain can aid their band alignment and affect the thermoelectric properties. Our results provide a combined band engineering strategy in which alloying and lattice strain effects synergistically act to improve the PF and μ_w near room temperature. In addition, the thermal conductivity values were systematically reduced due to the suppression of bipolar contribution and strengthened alloy scattering of phonons. Consequently, the maximum zT value almost reached 1.2 at 423 K for $Mg_{3.2}Bi_{1.498}Sb_{0.5}Te_{0.002}Cu_{0.005}$. Surprisingly, a zT value of 1.1 at 300 K was also achieved for $Mg_{3.2}Bi_{1.598}Sb_{0.4}Te_{0.002}Cu_{0.005}$. Our work demonstrates that Mg_3Bi_2-based compounds have great potential to be a game-changer in the near-room temperature cooling applications.

2. Results and Discussion

Figure 1a shows the powder X-ray diffraction (XRD) patterns of the $Mg_{3.2}Bi_{1.998-x}Sb_xTe_{0.002}Cu_{0.005}$ (Sbx, x = 0.0, 0.1, 0.2, 0.3, 0.4, and 0.5) sintered compounds. The XRD patterns indicate that the major diffraction peaks are well indexed to the trigonal structure of Mg_3Bi_2 (space group No. 164, α-La_2O_3-type structure). In previous studies, it was revealed that the dopant Cu atoms prefer occupying interstitial sites to Mg sites in the Mg_3Sb_2-based system and the minor addition of Cu does not change the lattice parameters.[23] Meanwhile, we confirmed Bi impurity peaks in the XRD patterns as shown in Figure 1a, but the intensities of Bi phase gradually decrease with increasing Sb concentration. It seems that the peak disappeared in Sb0.5 compound. It is also known that under high-temperature conditions, the secondary phase of Bi begins to appear at temperatures above 723K, resulting in the reduction in microscopic strain.[23,34] The lattice parameters in both a and c axes show a slowly decreasing trend with the content of Sb as presented in Figure 1b, because the ionic radius of Sb^{3-} is smaller than that of Bi^{3-}.

Scanning electron microscopy (SEM) images show the fractured surface of the compounds (Sb0.0, Sb0.3, and Sb0.5), as presented in **Figure 2a-c**. As the Sb content increases, the grain size becomes gradually smaller compared to that of Sb0.0. It is speculated that this is closely related to the fact that the melting point of Mg_3Sb_2 (≈1500 K) is much higher than Mg_3Bi_2 (≈1094 K) while all samples were sintered under the same temperature conditions. In other words, the grain morphology can be adjusted depending on the Sb content. Meanwhile, all samples have something in common feature which is a lot of nanopores as shown in Figure 2. The nanopores are formed by evaporation of excess Mg during the high-temperature sintering process and the pore's size gradually becomes smaller with increasing the amount of Sb. Despite the large number of nanopores, the relative density values of all samples are greater than 96%. This means that only virtually any excess Mg atoms ($Mg_{3.2}$-based system) are evaporated during the sintering process. Figure S1 (Supporting Information) shows the High-angle annular dark-field scanning transmission electron microscopy (HADDF-STEM) images and energy-dispersive X-ray spectroscopy (EDS) elemental maps for the Sb 0.5 Sample. The HADDF-STEM images show the regions (indicated by green arrows) that can be considered nanopores less than 200 nm in size. The EDS elemental maps reveal different contrasts, allowing the identification of an empty nanopore. In addition, the real chemical compositions measured by energy-dispersive X-ray spectroscopy (EDS) for all samples are shown in Table S2 (Supporting Information). The atomic percentage values of the major elements in our system (Mg, Bi, and Sb) show reasonable variations. The values of Mg are almost maintained, while the values of Bi and Sb show linear changes with increasing Sb content. Despite Mg evaporation issue, the target chemical composition ratios ($Mg_3(Bi, Sb)_2$) are relatively well preserved.

Figure 3a-c shows the low-magnification transmission electron microscopy (TEM) images and the inverse fast Fourier transform (IFFT) image of Sb0.5 compound. Ripple-like contrast

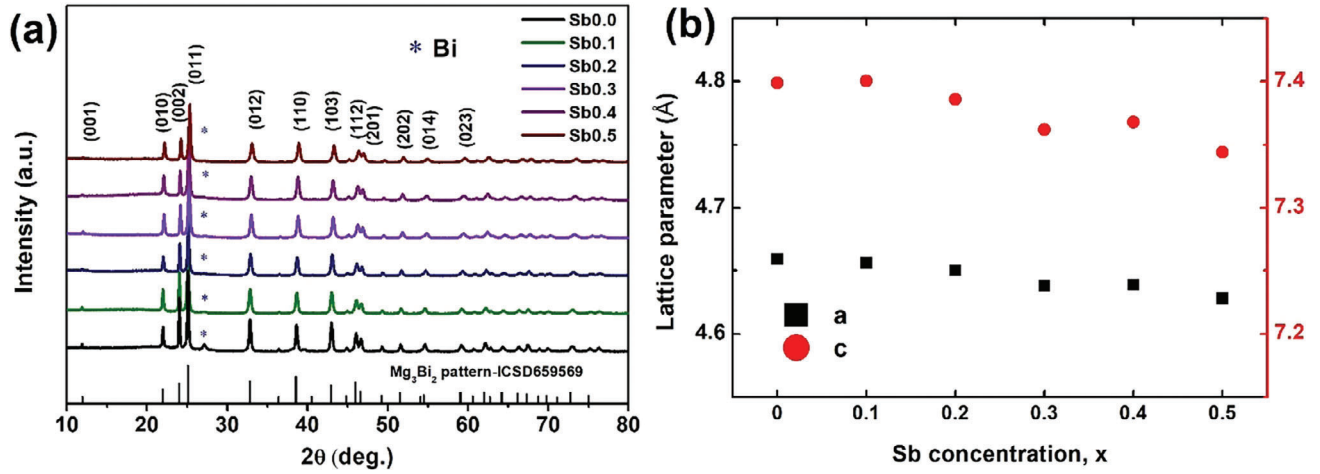

Figure 1. a) Powder X-ray diffraction patterns and b) lattice parameters of $Mg_{3.2}Bi_{1.998-x}Sb_xTe_{0.002}Cu_{0.005}$ (x = 0.0, 0.1, 0.2, 0.3, 0.4, and 0.5) compounds.

patterns associated with lattice distortion are easy to spot in both the low-magnification images (Figure 3a,b). It can be inferred that the formation of ripples is likely due to strong strain caused by the nanopores inside the lattice.[35,36] One of the probable strain formation mechanisms is the differential expansion or contraction of the lattice near the nanopores when heating or cooling the material during the sintering, resulting in strong lattice strain. The inverse FFT image shows the dense dislocation array (marked as ⊥) caused by internal stress in the ripple shape lattice fringe, as presented in Figure 3c. To analyze the lattice strain caused by the strong stress, high-quality high-resolution TEM images are focused. Figure 3e (enlarged TEM image of the marked regions shown in Figure 3d) shows that the lattice fringes are clearly divided into the ripple and non-ripple areas. Based on a geometric phase analysis (GPA), which is a semiquantitative lattice image processing approach, spatially distributed strain fields can be mapped as shown in Figure 3g,h. Large lattice strain fluctuations exist in the ripple region containing a lot of dislocations and it is also confirmed that the ripple and non-ripple areas contrast sharply by strain mapping. This means that there is strong stress in that lattice fringe. Furthermore, the electron diffraction pattern of the compound along the [122] zone axis (marked with yellow solid circles in Figure 3f) displays elongated diffraction spots along the crystal planes, indicating strong lattice distortions or stress in the matrix. Consequently, the TEM observations clearly show the lattice strain due to strong stress, and it is strongly assumed that the lattice strain is formed by differential expansion or contraction by the nanopores created during the sintering. To support this assumption, we investigated the XRD patterns of excess-Mg and non-excess samples (Mg_3Bi_2 and $Mg_{3.2}Bi_2$)

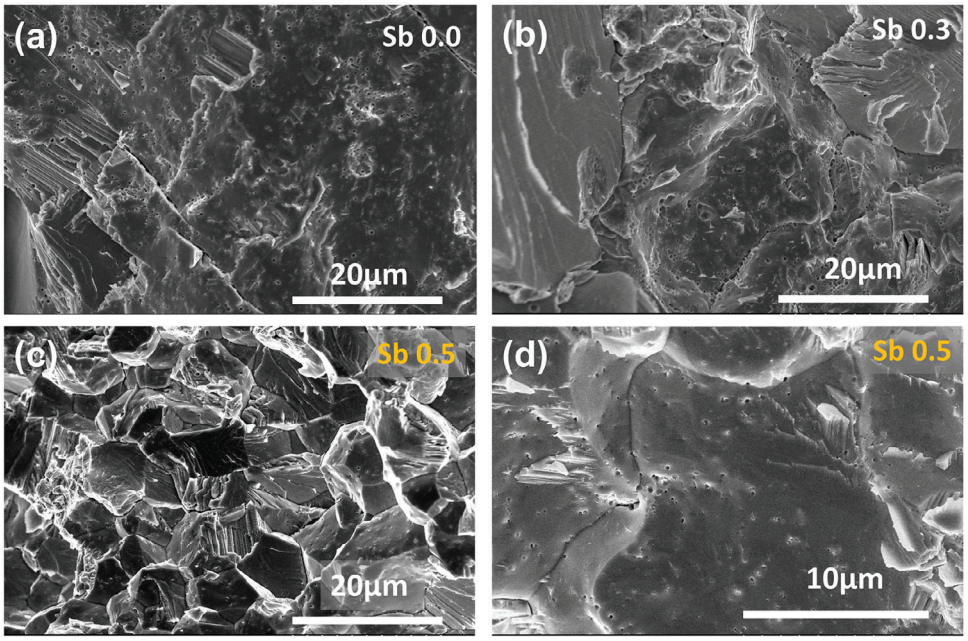

Figure 2. Scanning electron microscope images a–d) of $Mg_{3.2}Bi_{1.998-x}Sb_xTe_{0.002}Cu_{0.005}$ (x = 0.0, 0.3, and 0.5) compounds.

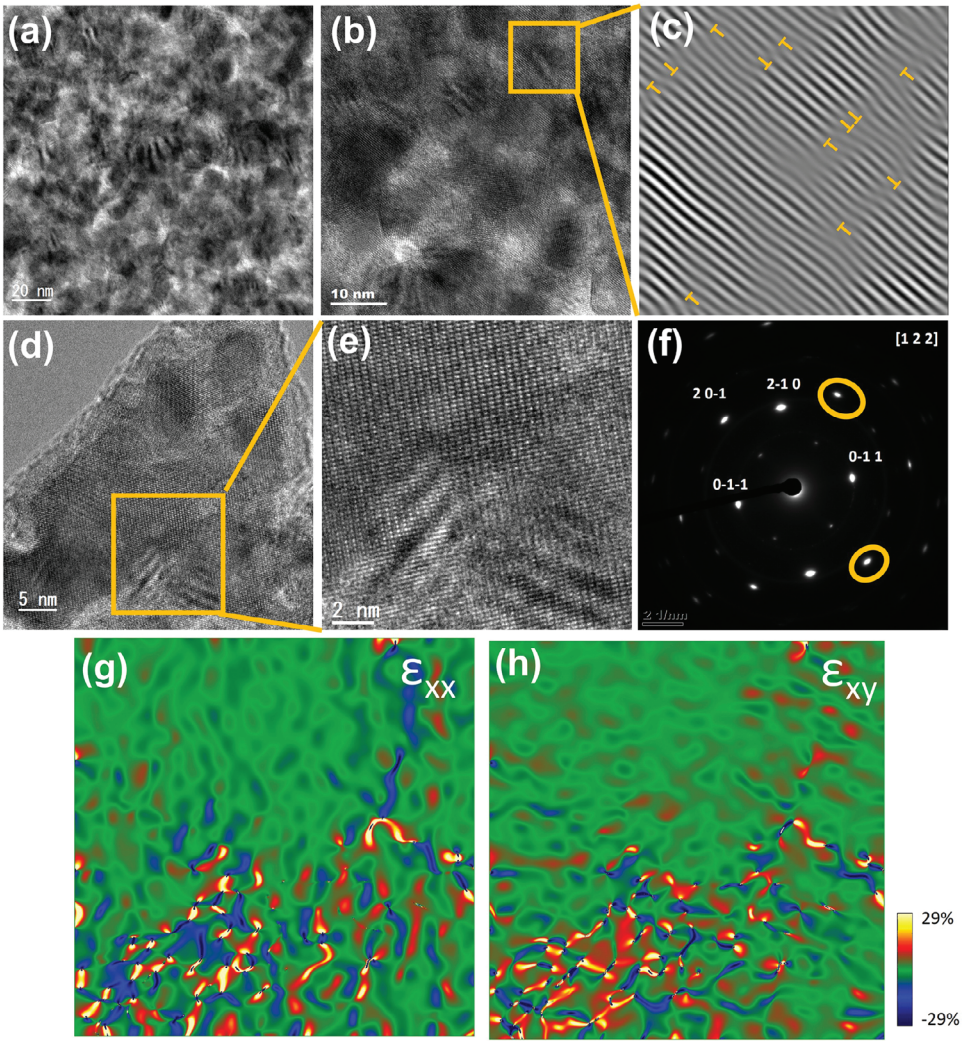

Figure 3. Microstructure of $Mg_{3.2}Bi_{1.998-x}Sb_xTe_{0.002}Cu_{0.005}$ (x = 0.5) compound: a,b) low magnification transmission electron microscopy images. c) Enlarged inverse fast Fourier transform (IFFT) image of the boxed region in (b). Dislocations indicated as yellow symbols are clearly shown. d) High resolution TEM image of specimen edge. e) Enlarged view of the boxed region in (d) including ripple shape lattice fringe. f) Electron diffraction pattern of the x = 0.5 sample along the [122] zone axis, displaying elongated diffraction spots. g,h) the corresponding strain mappings of the image (e) along the ϵ_{xx} *and* ϵxy *(color scale indicates −29% to 29% strain distribution)*.

because the nanopores come from excess-Mg sample during the sintering process as presented in Figure S2a (Supporting Information). In general, the XRD peak broadening was caused by lattice strain and decreased crystallite size. The Williamson-Hall relation provides information about the lattice strain and crystallite size from XRD patterns as shown in the following equation[37,38]:

$$\beta cos\theta = \frac{K\lambda}{r} + 4\sigma\, sin\theta \quad (1)$$

where λ is the incident X-ray wavelength, K is a dimensionless shape factor with a typical value of 0.9, r is the crystalline domain size, σ is the micro-strain fluctuation, θ is the diffraction angle, and β is the full width at half maximum (FWHM). Figure S2b (Supporting Information) shows $\beta cos\theta$ versus $4sin\theta$ plots for samples with and without excess Mg, in which the slope of regression line represents the strain component. The slope value of $Mg_{3.2}Bi_2$ increased slightly by ≈8% compared to the non-excess sample, which means that there is more lattice distortion inside the lattice in excess-Mg sample. To further support our claim, we investigated the microstructure of the fracture surface of $Mg_{3.2}Bi_2$ and Mg_3Bi_2 samples through SEM measurements as shown in Figure S3 (Supporting Information). In the Mg-excess sample in Figure S3d-f (Supporting Information), the nanopores can be seen to be formed in a lot of numbers, but in the non-excess system (Figure S3a-c, Supporting Information), the overall number of nanopores is significantly reduced. To be precise, not all nonpores have disappeared. This means that Mg atoms are still highly volatile at high-temperature sintering conditions. Nevertheless, it can be assumed that the significant change in the number of nanopores is one of the main factors in the formation of lattice strain. Furthermore, as shown in Figure S4 (Supporting Information), Bi particles (dark gray regions marked with orange arrow) as an

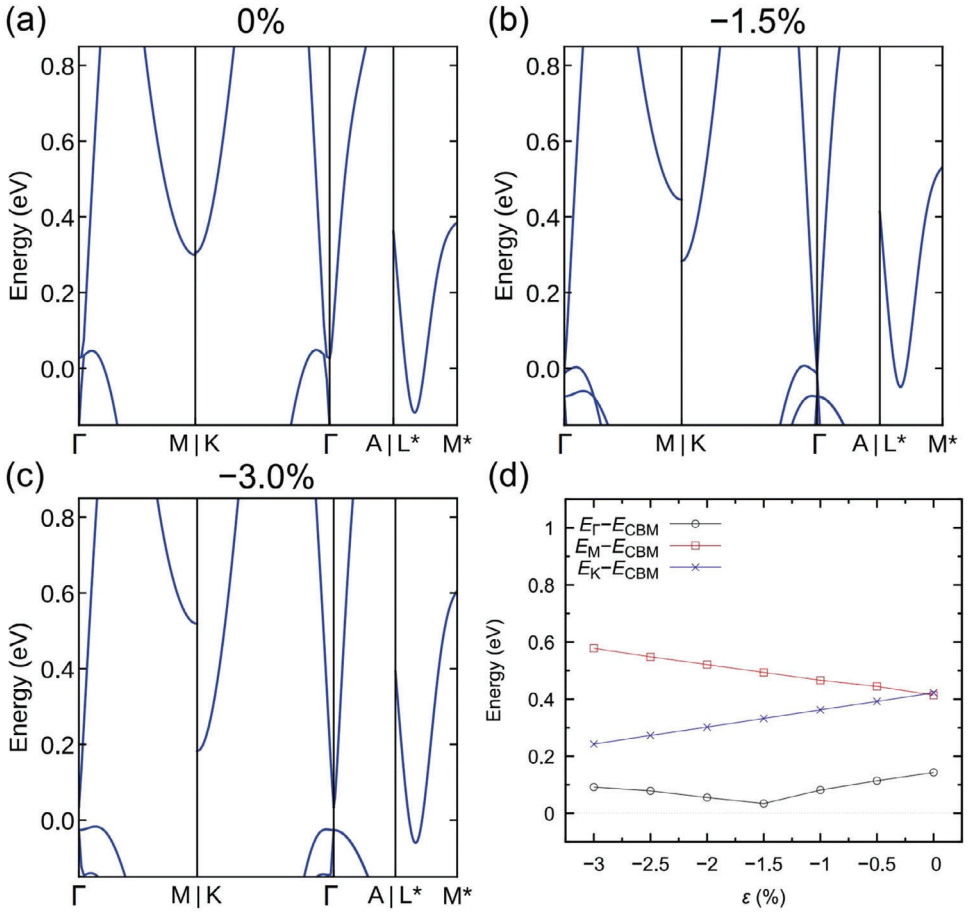

Figure 4. a–c) Calculated band structure of Mg_3Bi_2 compound under different strains. d) The band energy relations between conduction band minimum (CBM) and others (Γ, M and K band).

impurity secondary phase were found within the matrix. The size of the particles varies from a few micrometers to hundreds of nanometers. It can be expected that the Bi particles can easily aggregate together. Additionally, comparing the randomness of the distribution of Bi-particles (Figure S4, Supporting Information) and nanopores (Figure S3d,e, Supporting Information), it can be seen that the distribution of nanopores is more randomly distributed and the sizes of the nanopores are almost similar, which means that randomly distributed nanopores influence the strain more dominantly than the Bi impurity particles. Herein the minor added Cu in our system may cause additional lattice strain, but such an effect from Cu was not considered because of a very small portion of Cu compared to excess-Mg content. Based on these results, we propose that the nanopores created by excess-Mg during the sintering can strongly induce the lattice strain.

The crystal structure of Mg_3Bi_2 is composed of Mg^{2+} cation layer and $[Mg_2Bi_2]2^-$ anion layer and the layers are stacked along the c axis. The Mg atoms of the cation layer is located at vertex site of a single cell and can be easily evaporated during synthesis process, leading to the formation of Mg vacancy defects.[39] In addition, it is known that the position of the excess-Mg atoms favors some interstitial sites in the cation layer.[40] That is, in our system, it can be strongly assumed that the grain boundaries containing the nanopores created during the sintering are closely related to the Mg cation layer, and the formation of these nanopores causes the lattice strain. The strong stress can appear as the ripples on the plane of the lattice fringes, which means that biaxial strain can be applied to our system. Normally, the formation of such lattice strains can affect the carrier transport properties by causing electron-phonon interactions or by changing the electronic band structure.[41,42] To study the effect of biaxial strains on the electronic band structure of Mg_3Bi_2, density function theory (DFT) calculations considering the strain effect were performed. The biaxial strains were applied for the Mg_3Bi_2 unit cell according to the procedure described in Experimental Section. **Figure** 4a shows the band structure of unstrained Mg_3Bi_2, and Figure S2a–c (Supporting Information) shows unfolded effective band structure of alloyed compositions $Mg_3Bi_{2-x}Sb_x$ (x = 0.3125, 0.40625, and 0.5, respectively). The band structures indicate that the conduction band minimum is located at along the L*-M* line inside the first Brillouin zone with six-folded valley degeneracy while the valence band maximum is located near Γ point. Figure 4a shows that Mg_3Bi_2 has negative band gap or the band overlap. It is well known that DFT calculations tend to underestimate the band gap without any correction schemes, but the energy relationship within the conduction bands is relatively accurate. Nevertheless, even with increasing Sb content, there appears to be little qualitative difference in the band structure, except for a

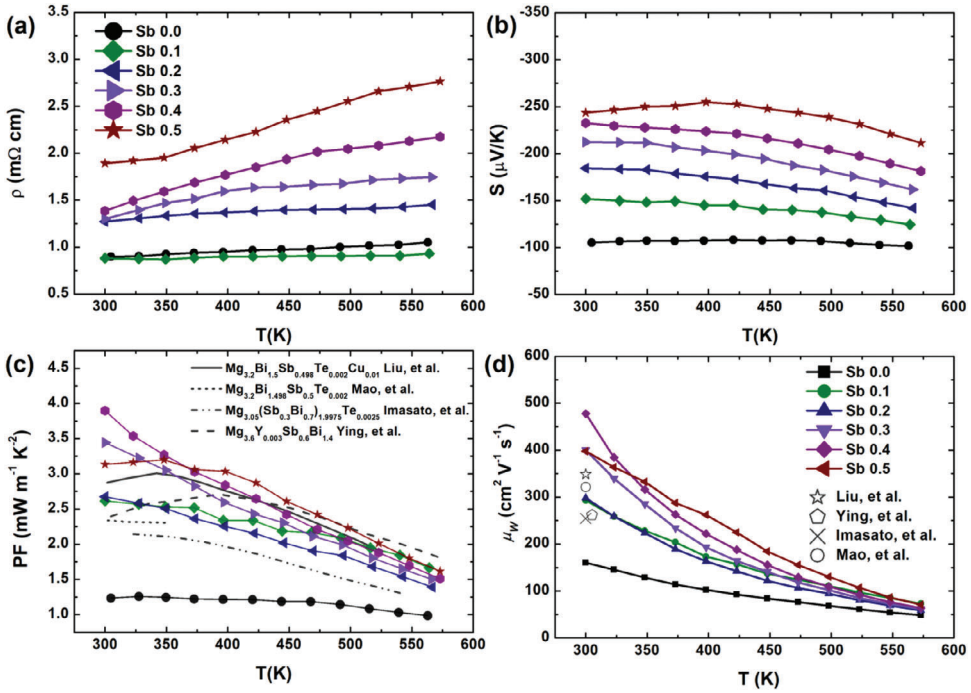

Figure 5. a) Temperature-dependent electrical resistivity $\rho(T)$, b) Seebeck coefficients $S(T)$, c) power factors PF and d) weighted mobility μ_w for $Mg_{3.2}Bi_{1.998-x}Sb_xTe_{0.002}Cu_{0.005}$ (x = 0.0, 0.1, 0.2, 0.3, 0.4, and 0.5) compounds in comparison with the data from Liu et al.[23] and Mao et al.[22] Imasato et al.[11] Ying et al.[24]

slight upward shift in the conduction band at Γ point, as shown in Figure S5 (Supporting Information). However, the applied strain causes significant changes in the band structure of Mg_3Bi_2, as presented in Figure 4b,c. Figure 4d represents the band energy relations between the conduction band minimum (CBM) and other bands. Especially, the energy difference between CBM and Γ band is minimized by −1.5% strain (≈0.03 eV). The difference values ($\Delta E_{\Gamma\text{-CBM}}$) decrease toward the minimum point with increasing the strain and then increase again but is still lower than the unstrained value (0.0%). When performing the calculation with a strain of −1.5% for the composition x = 0.3125, a similar reduction in the energy difference $\Delta E_{\Gamma\text{-CBM}}$ is also observed from 0.186 to 0.143 eV, as shown in Figure S6 (Supporting Information). Based on these results, it can be concluded that the strain modifies the band edge structure in the form of band alignment and can improve their carrier transport properties as a hidden role in the excess-Mg strained systems.

Figure 5a presents the temperature-dependent electrical resistivity $\rho(T)$ of $Mg_{3.2}Bi_{1.998-x}Sb_xTe_{0.002}Cu_{0.005}$ compounds. The $\rho(T)$ in all samples show degenerate-semiconducting or metallic behavior. Previous studies have shown that the minor addition of Cu not only reduces the thermal conductivity but also eliminates the extra scattering mechanism such as ionized impurities and grain boundaries scattering and allows the acoustic phonon scattering to dominate, which helps reduce the electrical resistivity with decreasing temperature.[23,40] This means that the effect of Cu addition is still being applied to our system. The $\rho(T)$ values are gradually increased with increasing the Sb content. This is because the Hall carrier concentrations listed in **Table 1** in the alloyed samples are steadily decreased at room temperature, and could also be associated with the gradual disappearance of semi-metallic properties with increasing Sb amount, which will be discussed in detail later.

Table 1. Hall carrier concentration n_H, Hall mobility μ_H, Seebeck coefficient S, reduced chemical potential η, weighted mobility μ_w, and density-of-state effective mass m_d^* of $Mg_{3.2}Bi_{1.998-x}Sb_xTe_{0.002}Cu_{0.005}$ (x = 0.0, 0.1, 0.2, 0.3, 0.4, and 0.5) compounds at 300 K.

Sb	n_H [10^{19} cm^{-3}]	$\lvert S\rvert$ [μV K^{-1}]	η	μ_H [cm^2 V^{-1} s^{-1}]	m_d^*/m_e	μ_w [cm^2 V^{-1} s^{-1}]
0.0	3.55	105	2.24	196	0.61	160
0.1	2.90	152	0.98	244	0.88	292
0.2	1.98	184	0.34	248	0.93	298
0.3	1.70	212	−0.13	280	1.1	400
0.4	1.50	233	−0.43	300	1.2	477
0.5	1.13	244	−0.60	292	1.1	398

The Seebeck coefficients $S(T)$ of all samples are displayed in Figure 5b. They have n-type properties with negative Seebeck coefficient values. The absolute values of $S(T)$ in the samples show systematic increasing trends with increasing the Sb content overall temperature range compared to the Sb0.0 sample. Overall, the $S(T)$ of the Sb-alloyed samples similarly tends to decrease with increasing temperature, except for slightly different curve of the Sb0.5 composition. It is well known that such $S(T)$ showing the decreasing trends is common in narrow band gap systems due to the increased bipolar contribution such as Bi_2Te_3-based systems. The systematic increase in the $S(T)$ with increasing Sb content can be referred to a change in the band structure. Although the band gap by our DFT calculation is underestimated, the increasing trend in band gap with increasing Sb content, including Sb-rich region,[43] can be observed (Figure S5d, Supporting Information). That is, in the case of the Sb0.5, the bipolar contribution at around room temperature decreases due to the increase in the band gap, and the maximum value of the $S(T)$ shifts toward higher temperature compared to the other samples. In particular, it is known that in Sb-rich $Mg_3(Sb,Bi)_2$ system, the $S(T)$ does not drop even at high temperature.[40,43] To indirectly prove the band gap opening, we investigated the magnetoresistance (MR) and Hall resistivity (ρ_{xy}) in the Sb0.0 and 0.5 samples at different temperatures in a magnetic field of up to 8 Tesla. The Mg_3Bi_2 compound have recently become known as nodal-line semimetal, a new type of topological.[25] It has also been reported that the large MR properties appear in even polycrystalline Mg_3Bi_2 compound.[26] The MR values for the Sb0.0 at 2K and 8 Tesla (Figure S7a, Supporting Information) show the dramatic increased value of ≈500% and are still unsaturated even at a magnetic field strength of up to 8 T. Electron-hole compensation and ultrahigh carrier mobility are typically required for large MR. In addition, due to the presence of electrons and holes, these topological semimetals typically have a high MR that does not saturate even in high magnetic fields. The magnetic field dependent Hall resistivity ρ_{xy} shows non-linear behavior in the Sb0.0, as presented in Figure S7c (Supporting Information), which means that this system is based on two carriers. In contrast, the Sb0.5 sample indicates much lower MR and linear ρ_{xy} in all temperature regions (Figure S4b,d, Supporting Information). This means that the single carrier transport can be more advantageous in this system. Therefore, the band gap in the Mg_3Bi_2-based systems can become larger as the Sb content increases.

The Hall carrier concentration n_H, Hall mobility μ_H, Seebeck coefficient S, reduced chemical potential η, weighted mobility μ_w, and density-of-state effective mass m_d^* of all samples at 300 K are listed in Table 1. The $n_H$values of the alloyed samples are systematically decreased to that of Sb0.5 from 3.55×10^{19} cm^{-3} to 1.13×10^{19} cm^{-3}. Typically, the n_H and μ_H are inversely proportional. The $\mu_H$values of the alloyed samples show a significant increasing trend with the Sb content. The m_d^* values from the experimental n_H dependent S have been estimated using the single parabolic band (SPB) model (Table 1). The n_H-dependent Seebeck coefficient can be calculated under acoustic phonon scattering using the SPB model derived from the Boltzmann transport equation.[44]

$$S = \frac{k_b}{e}\left(\frac{2F_1(\eta)}{F_0(\eta)} - \eta\right) \tag{2}$$

$$n_H = \frac{16\pi}{3}\left(\frac{2m_d^* k_b T}{h^2}\right)\left(\frac{(F_0(\eta))^2}{F_{-\frac{1}{2}}(\eta)}\right) \tag{3}$$

where $F_i(\eta)$ and η are Fermi integral of order i and the reduced Fermi energy ($\eta = E_F/k_bT$) and $F_i(\eta)$ is the ith order Fermi integral given by

$$F_i(\eta) = \int_0^\infty \frac{\epsilon^i}{1 + exp[\epsilon - \eta]} \tag{4}$$

where ϵ is the reduced energy. The estimated m_d^* values of the Sb-alloyed samples significantly increase compared to that of the Sb0.0. Although the η values gradually decrease with increasing Sb content, the maximum m_d^* value is shown in Sb0.4 sample and not in Sb0.5. This means that the chemical potential shifts to the edge of the density of state in the SPB system, but the slightly lower m_d^* value of Sb0.5 indicates further modification of the band structure. It was mentioned above that increasing the Sb content can cause the Γ band to shift upward as presented in Figure S5 (Supporting Information). This slight decrease in the m_d^* and μ_H of the Sb0.5 sample can be due to the chemical potential moving to the DOS edge and further away from the influence of the Γ band with the linear-like dispersion associated with high carrier mobility. That is, the upward deviation of the Γ band for the Sb0.5 means that the band alignment effect due to the strain is also reduced. In addition, the significant increase in effective mass values of the Sb-alloyed samples indicates a growing DOS.

The power factors PF are presented in Figure 5c. The PF values for the Sb-alloyed samples are higher than that of the Sb0.0 sample. It is noteworthy that the room temperature power factors of the Sb0.3, Sb0.4, and Sb0.5 samples have higher values than 3.0 mW m^{-1} K^{-2} and especially an ultrahigh value of the Sb0.4 sample even reaches ≈4.0 mW m^{-1} K^{-2}, which corresponds to the state-of-the-art value among the Mg_3Bi_2-based compounds. In addition, these ultrahigh values mean that the samples in this work are as good as those of Bi_2Te_3-based compounds[13,15,45,46] near room temperature. Therefore, the high-power factor values could be achieved in our work through various combined band engineering strategies, such as the band alignment by the strain, shifting the chemical potential, growing the electronic density of states with Sb content. The weighted mobility μ_w proportional to the PF values is a good direct indicator of the electronic transport quality of thermoelectric materials. Generally, the μ_w is a product of drift mobility and density of states effective mass and is also estimated from μ_H and m_d^*. Recently, Snyder et al. provided a simple equation to calculate μ_w from measured S and ρ within the single band assumption as in the following equation:[47]

$$\mu_w = 331\frac{cm^2}{Vs}\left(\frac{m\Omega\ cm}{\rho}\right)\left(\frac{T}{300K}\right)^{-3/2}\left[\frac{exp\left[\frac{|S|}{k_B/e} - 2\right]}{1 + exp\left[-5\left(\frac{|S|}{k_B/e} - 1\right)\right]} + \frac{\frac{3}{\pi^2}\frac{|S|}{k_B/e}}{1 + exp\left[5\left(\frac{|S|}{k_B/e} - 1\right)\right]}\right] \tag{5}$$

The obtained $\mu_w$values are shown in Figure 5d and Table 1. The $\mu_w$values of the Sb-alloyed samples are dramatically improved with Sb content at 300 K and sample and tend to be similar to

Table 2. Band parameters (effective mass m^*, deformation potential E_{def} (eV), weighted mobilityμ_w, for conduction band (CB) and valence band (VB), band gap and weighted mobility ratio A) of $Mg_{3.2}Bi_{1.998-x}Sb_xTe_{0.002}Cu_{0.005}$ (x = 0.0, 0.4, and 0.5) compounds at 300 K determined from the measured electronic transport properties using the two-band model.

Band parameters	Sb 0.0	Sb 0.4	Sb 0.5
CB m^*/m_e	0.678	1.19	1.09
VB m^*/m_e	0.295	0.295	0.295
$E_{def,\ CB}$ (eV)	22.1	10.4	11.9
$E_{def,\ VB}$ (eV)	12	12	12
Band gap (eV)	−0.013	0.1	0.125
$\mu_{w,CB}$ (cm^2/Vs)	138	322	282
$\mu_{w,VB}$ (cm^2/Vs)	103	105	106
A ($\mu_{w,CB}/\mu_{w,VB}$)	1.3	3.1	2.7

those of the power factor. The highest μ_w value among the samples is 477 $cm^2\ V^{-1}\ s^{-1}$ at the Sb0.4 sample. These are exceptionally enhanced values compared to previous reports,[11,22–24] as presented in Figure 5d. This indicates the good electronic quality of our synthesized samples. Additionally, it can also be strongly deduced that the decrease in the μ_w value of the Sb0.5 sample is due to the chemical potential moving away from the influence of the Γ band.

Since the Mg_3Bi_2-based compounds have a narrow band gap similar to the Bi_2Te_3 system, it is useful to consider the bipolar contribution to better understand the carrier transport behavior. **Table 2** lists quantitatively analyzed band parameters for the conduction band (CB) and valence band (VB) using two-band model based on the SPB model considering the bipolar contribution (details are described in the Supplemental Information).[44] The modeled individual Seebeck coefficients (S_i) and electrical conductivities (σ_i) (where $i = n$ and p for the CB and VB, respectively) for the CB and VB are fitted to the experimentally measured total S and σ using the following equation:

$$\sigma = \sigma_p + \sigma_n \tag{6}$$

$$S = \frac{\sigma_p S_p - \sigma_n S_n}{\sigma_p + \sigma_n} \tag{7}$$

Here, the deformation potential E_{def} and m^* values for the CB and VB were used as fitting parameters in two-band model. We have taken the valley degeneracy N_V of the CB and VB to be 6 and 1[14,31,39,41] respectively, and a longitudinal elastic modulus C_l of 40 GPa[33] and the band gap values from other work.[14] The m^*values of the Sb0.4 and Sb0.5 for the CB significantly increase compared to that of the Sb0.0 and the E_{def} values show decreasing trend with increasing the Sb content. We calculated the weighted mobilities $\mu_w (= \mu_0\ (m_d^*/m_0))$ of each band, where μ_0 is the non-degenerate mobility.

$$\mu_0 = \frac{e\pi\hbar^4 N_v^{5/3} v_l^2 d}{\sqrt{2} E_{def}^2 m_d^{*\ 5/2} (k_B T)^{3/2}} \tag{8}$$

where e, $\hbar$, d, and $k_B$are the electronic charge, reduced Planck's constant, material density, and Boltzmann constant, respectively. The $\mu_{w,CB}$ values of the Sb-alloyed samples are twice larger than that of the Sb0.0 at 300 K. In addition, the weighted mobility ratio A, which provides with indications about the more favorable carrier transport in this two-carrier system, are listed in Table 2. The value of 3.1 for the Sb0.4 sample is the highest, whereas the value for Sb0.5 slightly decreases at 300 K. Nevertheless, it can be concluded that these results for the Sb alloyed samples show that the bipolar contribution in this system is significantly reduced at room temperature.

The total thermal conductivities κ_{tot} of $Mg_{3.2}Bi_{1.998-x}Sb_xTe_{0.002}Cu_{0.005}$ samples are presented in **Figure 6a**, showing that the κ_{tot} values systematically decreased with increasing Sb content. In addition, the κ_{tot} values of all samples increase with increasing temperature over the entire temperature region, implying the presence of the bipolar contribution in this narrow band gap system. The total thermal conductivity can be divided into electronic, lattice, and bipolar contributions given by the following equation:

$$\kappa_{tot} = \kappa_e + \kappa_{bp} + \kappa_{lat} \tag{9}$$

where κ_e,κ_{bp} and κ_{lat} are the electronic, bipolar, and lattice thermal conductivities, respectively. The κ_e can be obtained from the relation $\kappa_e = LT/\rho$, where L, T, and ρ are Lorenz number, absolute temperature, and electrical resistivity, respectively. The Lorenz number is given by $L_0 = 2.45 \times 10^{-8}$ W Ω K^{-2} in the conventional metallic system. However, the metallic Lorentz number is not applicable in electronic correlated materials and degenerated semiconductors. Thus, the Lorentz number is estimated using the two-band model. The κ_e values of the Sb0.0, Sb0.4, and Sb0.5 are presented in Figure 6b and decrease with Sb content. The κ_{bp} can be described by the following equation:

$$\kappa_{bp} = \left(S_p^2 \sigma_p + S_n^2 \sigma_n - \frac{(S_p \sigma_p + S_n \sigma_n)^2}{\sigma} \right) T \tag{10}$$

Figure 6c shows that the temperature-dependent κ_{bp} values decrease with increasing Sb content over the entire temperature range. The difference between the κ_{bp} values of the Sb0.0 and Sb0.5 becomes larger with increasing temperature, which suggests that the bipolar contribution can be suppressed at high temperatures by the enlarged band gap. The κ_{lat} values of the Sb-alloyed samples (Sb0.4 and Sb0.5) are greatly lowered compared to that of the Sb0.0 sample, as presented in Figure 6d. Typically, alloying has the advantage of greatly reducing thermal conductivity because the changes in the mass and size between Bi and Sb atoms help to scatter phonons. In our system, it can be assumed that alloy or point defect scattering of phonons is dominant among the phonon transport mechanisms. Additionally, according to the alloy scattering model, there is little change in the lattice thermal conductivity value between highly alloyed compositions.[48] Figure 6d shows that the reduced κ_{lat} values of Sb0.4 sample have little difference compared to Sb0.5 because they have already reached the minimized region due to sufficient alloy scattering effect. In other words, our results show that the increased disorder in the atomic configuration plays an

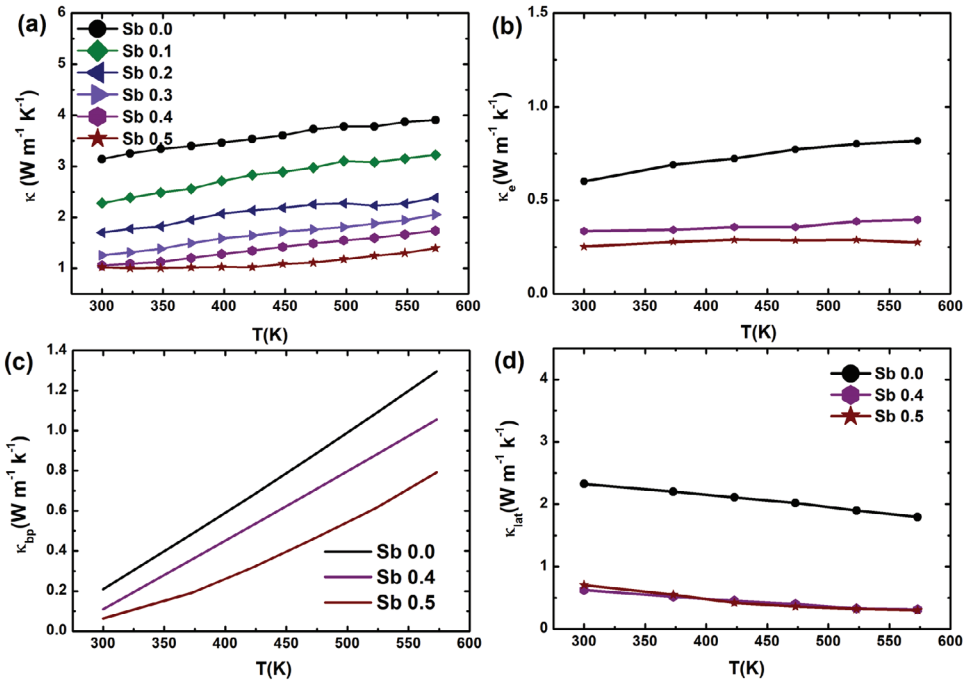

Figure 6. a) Temperature-dependent total thermal conductivity κ_{tot} of $Mg_{3.2}Bi_{1.998-x}Sb_xTe_{0.002}Cu_{0.005}$ (x = 0.0, 0.1, 0.2, 0.3, 0.4, and 0.5) compounds. b) The electronic thermal conductivity κ_e, c) bipolar thermal conductivity κ_{bp}, and d) lattice thermal conductivity for $Mg_{3.2}Bi_{1.998-x}Sb_xTe_{0.002}Cu_{0.005}$ (x = 0.0, 0.4, and 0.5) compounds.

important role in lowering the lattice thermal conductivity. Therefore, it can be concluded that the κ_{tot} with increasing Sb content is lowered by strengthening alloy scattering of phonons and suppressing the bipolar contribution.

The temperature-dependent zT values for all samples are presented in **Figure** 7a. The high power factor and low lattice thermal conductivity positively affect the zT values of Sb-alloyed samples, which exhibit significantly high values. The maximum zT values of the Sb0.4 and Sb0.5 reach 1.1 at 300 K and ≈1.2 at 423 K, respectively. The temperature dependent zT in the Sb 0.5 sample shows a dome shape compared to the others because the bipolar contribution is further suppressed up to high temperatures. Unfortunately, it can be judged that the Sb0.4 sample with high performance near room temperature is unable to overcome the bipolar contribution at higher temperatures compared to that of the Sb0.5. Nonetheless, these results demonstrate the thermoelectric performance that is superior to those of Mg_3Bi_2-based systemsas well as Bi_2Te_3-based compounds and suggest that strategies to further suppress the bipolar contribution in this Bi-rich system may be highly suitable in future studies to maximize the thermoelectric performance near room temperature. Figure 7b shows the average zT (zT_{avg}) values over the temperature range

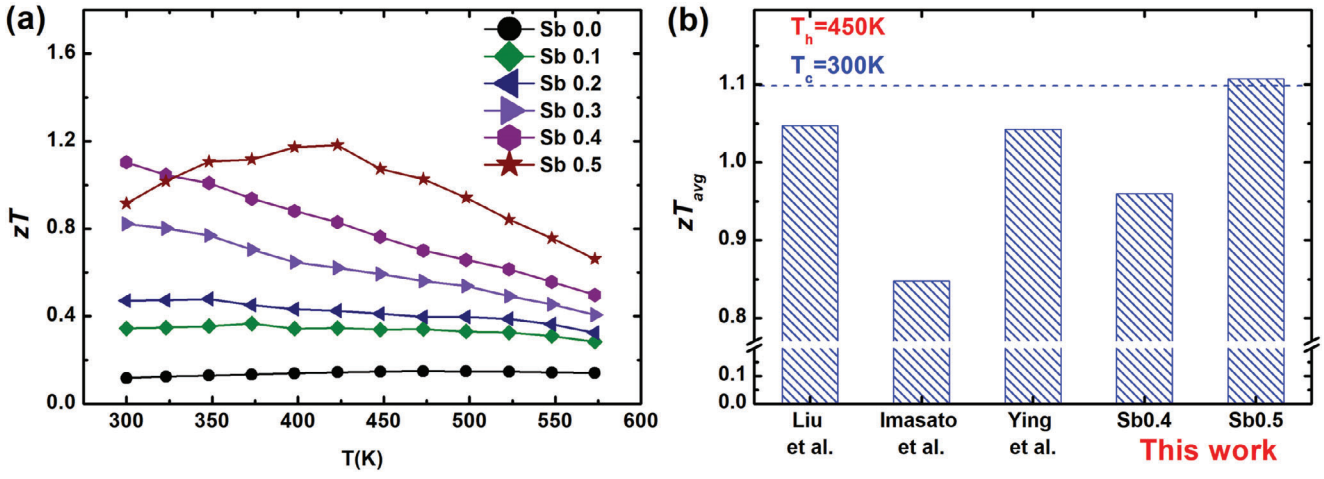

Figure 7. a) Temperature-dependent zT values for $Mg_{3.2}Bi_{1.998-x}Sb_xTe_{0.002}Cu_{0.005}$ (x = 0.0, 0.1, 0.2, 0.3, 0.4, and 0.5) compounds. b) average zT (zT_{avg}) values in comparison with the data from Liu et al.[23] and Imasato et al.[11] Ying et al.[24]

from 300 to 450 K. The zT_{avg} values of above 1.1 in this work are superior in comparison with some other reports.[11,23,24] As a result, our results demonstrate the great potential of the Mg_3Bi_2-based compounds to replace the unsurpassed Bi_2Te_3-based materials which possess a long history for near-room temperature applications.

3. Conclusion

In summary, this study suggests that the multiple band engineering approaches to control the electronic properties such as the lattice strain effect, increasing the band gap, growing the density of state, and shifting the chemical potential can promote thermoelectric performance. Especially, it was revealed through the microstructural analysis and the DFT calculation that the nanopores created by the evaporation of excess Mg affect the lattice strain, and such strain can lead to the alignment of the conduction band minimum and the Γ band edge, thereby optimizing the band structure. The increased Sb content also optimizes their electrical transport properties, achieving leading-edge values exceeding 3.0 mW m^{-1} K^{-2} near room temperature. In addition, the significant reduction in total thermal conductivity is due to two factors: suppression of the bipolar contribution and promoting alloy scattering of phonons with increasing Sb content. As a result, the highest zT values of 1.1 and ≈1.2 at 300 and 423 K are achieved in $Mg_{3.2}Bi_{1.998-x}Sb_xTe_{0.002}Cu_{0.005}$ (x = 0.4 and 0.5) compounds, respectively. Furthermore, the zT_{avg} of above 1.1 at 300–450 K is recorded in $Mg_{3.2}Bi_{1.498}Sb_{0.5}Te_{0.002}Cu_{0.005}$ compound, which is better than other reported Mg_3Bi_2-based materials. Therefore, we conclude that the synergistic band structure engineering is an appropriate way to dramatically improve the thermoelectric performance in this system in the important temperature region near room temperature. Thereby, this work showcases the great potential of the Mg_3Bi_2-based compounds for room-temperature application to replace Bi_2Te_3-based materials.

4. Experimental Section

Materials Synthesis: High-purity elements of Mg (99.95%), Bi (99.999%), Sb (99.999%), Te (99.999%), Cu (99.9%) were directly weighed according to the nominal composition $Mg_{3.2}Bi_{1.998-x}Sb_xTe_{0.002}Cu_{0.005}$ (Sbx, x = 0.0, 0.1, 0.2, 0.3, 0.4, and 0.5) and then loaded into the stainless-steel jar in the glovebox under an argon atmosphere and then subjected to high-energy milling process (SPEX-SamplePrep 8000 Mixer Mill). The ball-milled powder was directly loaded into a graphite die with 10 mm diameter in the glovebox and then sintered by spark plasma sintering (SPS, Fuji Electronic Industrial Co. SPS-1080) at 973 K for 10 min under a uniaxial pressure of 60 MPa.

Characterizations: The X-ray diffraction was performed by Cu Kα radiation (XRD, Rigaku SmartLab3) for phase and structure investigation. A microstructural investigation was characterized using a field emission scanning electron microscope (FE-SEM, Hitachi S-4800). The sample was prepared by focused ion beam (FIB) (Hitachi FB-2000S) method for transmission electron microscopy observations using a beam of focused high-energy gallium ions. Scanning Transmission Electron Microscopy (STEM) was conducted using a JEOL JEM-3100FEF, operating at an acceleration voltage of 300 keV.

The Seebeck coefficient and electrical conductivity were measured by the four-probe method using the commercial thermoelectric measurement system (ADVANCE RIKO ZEM-3). The thermal conductivity was obtained from the relation of $\kappa_{tot} = DC_pd$, where D, C_p, and d are the thermal diffusivity coefficient, specific heat, and sample density, respectively. The thermal diffusivity coefficient D and the specific heat C_p were measured for the disk sample by a laser flash method (NETZSCH LFA-467) with Pyroceram 9606 disk as a reference sample. The sample density d was determined by the Archimedes method. The temperature-dependent Hall-resistivity and electrical resistivity were carried out by four-probe contact method using the physical property measurement system (Quantum Design PPMS) with sweeping magnetic field from −8 to +8 T. The Hall carrier concentrations were obtained by the relation of $n_H = -1/(R_He)$, $R_H = \rho_{xy}/H$ where R_H, e, ρ_{xy}, and H are Hall coefficient, electronic charge, Hall resistivity, and an applied magnetic field, respectively.

Computational Methods: The DFT calculations were performed using Quantum ESPRESSO package with projector augmented wave pseudopotentials.[49–51] The generalized gradient approximation functional with Peudew–Burke–Ernzerhof parametrization (GGA-PBE)[52] was chosen for the exchange and correlation potentials. Spin-orbit coupling was not considered in the present study. To model the alloying in (Sb,Bi)-site in $Mg_3(Sb,Bi)_2$, the special quasirondom structure (SQS) method implemented in the Alloy Theoretical Autometed Toolkit (ATAT), was used.[53] $4 \times 4 \times 2$ supercell was created with 160 atoms ($Mg_{96}Sb_{64}$) from the primitive cell of Mg_3Sb_2, and substituted Bi for Sb using the SQS algorithm according to compositions of (Sb, Bi) = (10, 54), (13, 51), (16, 48), which correspond to $x = 0.3125$, 0.40625, 0.5 in $Mg_3Sb_xBi_{2-x}$, respectively. The experimentally determined lattice parameters were used and atomic positions were fully relaxed without considering symmetry until the residual forces became less than 10^{-3} eV Å^{-1}. The cutoff energy of 80 Ry for the plane wave basis and $4 \times 4 \times 4$ k-grid were used for the structure relaxation. The effective band structures of the supercells with alloyed compositions in the primitive Brillouin zone were obtained by using the band unfolding method implemented in BandUP code.[54] The band structures considering the effect of biaxial strain were also calculated. The strain was defined as $\epsilon = (\alpha_{strain}/\alpha_0 - 1) \times 100(\%)$, where α_{strain} is the strained lattice constant, and α_0 is the unstrained lattice constant. The compressive strains (0.0–−3.0%) were applied for in-plane (a and b axes) and in turn out-of-plane (c-axis) lattice constant was optimized by DFT calculations (the strained lattice constants are listed in Table S1, Supporting Information), and atomic positions were fully relaxed after applying the strains. The band structures were calculated for each straind structure.

Supporting Information

Supporting Information is available from the Wiley Online Library or from the author.

Acknowledgements

This research was supported by JST Mirai Program, Japan (grant number JPMJMI19A1).

Conflict of Interest

The authors declare no conflict of interest.

Data Availability Statement

The data that support the findings of this study are available from the corresponding author upon reasonable request.

Keywords

band engineering, lattice strain, Mg_3Bi_2, thermoelectric performance

Received: April 24, 2024
Revised: July 11, 2024
Published online: August 1, 2024

[1] L. E. Bell, *Science* **2008**, *321*, 1457.
[2] T. Hendricks, T. Caillat, T. Mori, *Energies* **2022**, *15*, 7307.
[3] B. Poudel, Q. Hao, Y. Ma, Y. Lan, A. Minnich, B. Yu, X. Yan, D. Wang, A. Muto, D. Vashaee, X. Chen, J. Liu, M. S. Dresselhaus, G. Chen, Z. Ren, *Science* **2008**, *320*, 634.
[4] A. Pakdel, A. U. Khan, F. Pawula, S. Hébert, T. Mori, *Adv. Mater. Inter.* **2022**, *9*, 2200785.
[5] L. Hu, T. Zhu, X. Liu, X. Zhao, *Adv Funct. Mater.* **2014**, *24*, 5211.
[6] G. Jiang, J. He, T. Zhu, C. Fu, X. Liu, L. Hu, X. Zhao, *Adv. Funct. Mater.* **2014**, *24*, 3776.
[7] X. Lou, S. Li, X. Chen, Q. Zhang, H. Deng, J. Zhang, D. Li, X. Zhang, Y. Zhang, H. Zeng, G. Tang, *ACS Nano* **2021**, *15*, 8204.
[8] Y. Wu, Z. Chen, P. Nan, F. Xiong, S. Lin, X. Zhang, Y. Chen, L. Chen, B. Ge, Y. Pei, *Joule* **2019**, *3*, 1276.
[9] L. Xu, Y. Xiao, S. Wang, B. Cui, D. Wu, X. Ding, L.-D. Zhao, *Nat. Commun.* **2022**, *13*, 6449.
[10] Y. Pei, H. Wang, G. J. Snyder, *Adv. Mater.* **2012**, *24*, 6125.
[11] K. Imasato, S. D. Kang, G. J. Snyder, *Energy Environ. Sci.* **2019**, *12*, 965.
[12] Y. Pei, A. D. LaLonde, N. A. Heinz, X. Shi, S. Iwanaga, H. Wang, L. Chen, G. J. Snyder, *Adv. Mater* **2011**, *23*, 5674.
[13] H. Cho, S. Y. Back, J. H. Yun, S. Byeon, H. Jin, J.-S. Rhyee, *ACS Appl. Mater. Interfaces* **2020**, *12*, 38076.
[14] Y. Lin, M. Wood, K. Imasato, J. J. Kuo, D. Lam, A. N. Mortazavi, T. J. Slade, S. A. Hodge, K. Xi, M. G. Kanatzidis, *Energy Environ. Sci.* **2020**, *13*, 4114.
[15] H. Cho, J.-H. Yun, S. Y. Back, J.-S. Lee, N. Kang, Y.-I. Jang, J. Lim, J.-H. Son, J.-Y. Park, J. Kim, *J. Alloys Compd.* **2021**, *888*, 161572.
[16] F. Ahmed, N. Tsujii, T. Mori, *J. Mater. Chem. A* **2017**, *5*, 7545.
[17] S. Hébert, R. Daou, A. Maignan, S. Das, A. Banerjee, Y. Klein, C. Bourgès, N. Tsujii, T. Mori, *Sci. Technol. Adv. Mater.* **2021**, *22*, 583.
[18] H. J. Goldsmid, *Materials* **2014**, *7*, 2577.
[19] J. Pei, B. Cai, H.-L. Zhuang, J.-F. Li, *Nat. Sci. Rev.* **2020**, *7*, 1856.
[20] H. Tamaki, H. K. Sato, T. Kanno, *Adv. Mater.* **2016**, *28*, 10182.
[21] X. Shi, T. Zhao, X. Zhang, C. Sun, Z. Chen, S. Lin, W. Li, H. Gu, Y. Pei, *Adv. Mater.* **2019**, *31*, 1903387.
[22] J. Mao, H. Zhu, Z. Ding, Z. Liu, G. A. Gamage, G. Chen, Z. Ren, *Science* **2019**, *365*, 495.
[23] Z. Liu, W. Gao, H. Oshima, K. Nagase, C.-H. Lee, T. Mori, *Nat. Commun.* **2022**, *13*, 1120.
[24] P. Ying, L. Wilkens, H. Reith, N. P. Rodriguez, X. Hong, Q. Lu, C. Hess, K. Nielsch, R. He, *Energy Environ. Sci.* **2022**, *15*, 2557.
[25] T. Chang, I. Pletikosic, T. Kong, G. Bian, A. Huang, J. Denlinger, S. K. Kushwaha, B. Sinkovic, H. Jeng, T. Valla, W. Xie, R. J. Cava, *Adv. Sci.* **2019**, *6*, 1800897.
[26] T. Feng, P. Wang, Z. Han, L. Zhou, W. Zhang, Q. Liu, W. Liu, *Adv. Mater.* **2022**, *34*, 2200931.
[27] Y. Pei, X. Shi, A. LaLonde, H. Wang, L. Chen, G. J. Snyder, *Nature* **2011**, *473*, 66.
[28] Y. Xiao, D. Wang, Y. Zhang, C. Chen, S. Zhang, K. Wang, G. Wang, S. J. Pennycook, G. J. Snyder, H. Wu, L.-D. Zhao, *J. Am. Chem. Soc.* **2020**, *142*, 4051.
[29] G. Tan, L.-D. Zhao, M. G. Kanatzidis, *Chem. Rev.* **2016**, *116*, 12123.
[30] K. Imasato, S. D. Kang, S. Ohno, G. J. Snyder, *Mater. Horiz.* **2018**, *5*, 59.
[31] Y. Pan, M. Yao, X. Hong, Y. Zhu, F. Fan, K. Imasato, Y. He, C. Hess, J. Fink, J. Yang, *Energy Environ. Sci.* **2020**, *13*, 1717.
[32] M. Wood, K. Imasato, S. Anand, J. Yang, G. J. Snyder, *J. Mater. Chem. A* **2020**, *8*, 2033.
[33] I. T. Witting, T. C. Chasapis, F. Ricci, M. Peters, N. A. Heinz, G. Hautier, G. J. Snyder, *Adv. Elect. Mater.* **2019**, *5*, 1800904.
[34] L. R. Jørgensen, J. Zhang, C. B. Zeuthen, B. B. Iversen, *J. Mater. Chem. A* **2018**, *6*, 17171.
[35] S. Ahmed, A. Pokle, S. Schweidler, A. Beyer, M. Bianchini, F. Walther, A. Mazilkin, P. Hartmann, T. Brezesinski, J. Janek, K. Volz, *ACS Nano* **2019**, *13*, 10694.
[36] K. Elibol, T. Susi, O. Maria, B. C. Bayer, T. J. Pennycook, N. McEvoy, G. S. Duesberg, J. C. Meyer, J. Kotakoski, *Nanoscale* **2017**, *9*, 1591.
[37] G. K. Williamson, W. H. Hall, *Acta Metall.* **1953**, *1*, 22.
[38] H. Cho, S. Y. Back, J. H. Kim, O. Inturu, H. S. Lee, J.-S. Rhyee, *RSC Adv.* **2019**, *9*, 4190.
[39] S. Ohno, K. Imasato, S. Anand, H. Tamaki, S. D. Kang, P. Gorai, H. K. Sato, E. S. Toberer, T. Kanno, G. J. Snyder, *Joule* **2018**, *2*, 141.
[40] Z. Liu, N. Sato, W. Gao, K. Yubuta, N. Kawamoto, M. Mitome, K. Kurashima, Y. Owada, K. Nagase, C.-H. Lee, *Joule* **2021**, *5*, 1196.
[41] S. Ning, S. Huang, Z. Zhang, N. Qi, M. Jiang, Z. Chen, X. Tang, *J. Materiomics* **2022**, *8*, 1086.
[42] J. Zhang, L. Song, G. K. Madsen, K. F. Fischer, W. Zhang, X. Shi, B. B. Iversen, *Nat. Commun.* **2016**, *7*, 10892.
[43] L. Wang, N. Sato, Y. Peng, R. Chetty, N. Kawamoto, D. H. Nguyen, T. Mori, *Adv. Energy Mater.* **2023**, *13*, 2301667.
[44] D. M. Rowe, *Materials, Preparation, and Characterization in Thermoelectrics*, CRC Press, Boca Raton, Florida **2017**.
[45] L. Lou, J. Yang, Y. Zhu, H. Liang, Y. Zhang, J. Feng, J. He, Z. Ge, L. Zhao, *Adv. Sci.* **2022**, *9*, 2203250.
[46] K. H. Lee, H.-S. Kim, S. Choo, W. H. Shin, J.-H. Lim, S. W. Kim, S. Kim, *Scr. Mater.* **2020**, *186*, 357.
[47] G. J. Snyder, A. H. Snyder, M. Wood, R. Gurunathan, B. H. Snyder, C. Niu, *Adv. Mater.* **2020**, *32*, 2001537.
[48] R. Gurunathan, R. Hanus, G. J. Snyder, *Mater. Horiz.* **2020**, *7*, 1452.
[49] P. Giannozzi, S. Baroni, N. Bonini, M. Calandra, R. Car, C. Cavazzoni, D. Ceresoli, G. L. Chiarotti, M. Cococcioni, I. Dabo, *J. Phys.: Condens. Matter* **2009**, *21*, 395502.
[50] P. Giannozzi, O. Andreussi, T. Brumme, O. Bunau, M. B. Nardelli, M. Calandra, R. Car, C. Cavazzoni, D. Ceresoli, M. Cococcioni, *J. Phys.: Condens. Matter* **2017**, *29*, 465901.
[51] P. E. Blöchl, *Phys. Rev. B* **1994**, *50*, 17953.
[52] J. P. Perdew, K. Burke, M. Ernzerhof, *Phys. Rev. Lett.* **1996**, *77*, 3865.
[53] A. Van De Walle, *Calphad* **2009**, *33*, 266.
[54] P. V. C. Medeiros, S. Stafström, J. Björk, *Phys. Rev. B* **2014**, *89*, 041407.